



# Prevention of excessive scar formation using nanofibrous meshes made of biodegradable elastomer poly(3-hydroxybutyrate-co-3-hydroxyvalerate)

Hye Sung Kim<sup>1,2\*</sup>, Junyu Chen<sup>3,4\*</sup>, Lin-Ping Wu<sup>5</sup>, Jihua Wu<sup>6</sup>, Hua Xiang<sup>3,4</sup>, Kam W Leong<sup>1</sup> and Jing Han<sup>3,4</sup> 

## Abstract

To reduce excessive scarring in wound healing, electrospun nanofibrous meshes, composed of haloarchaea-produced biodegradable elastomer poly(3-hydroxybutyrate-co-3-hydroxyvalerate) (PHBV), are fabricated for use as a wound dressing. Three PHBV polymers with different 3HV content are used to prepare either solution-cast films or electrospun nanofibrous meshes. As 3HV content increases, the crystallinity decreases and the scaffolds become more elastic. The nanofibrous meshes exhibit greater elasticity and elongation at break than films. When used to culture human dermal fibroblasts in vitro, PHBV meshes give better cell attachment and proliferation, less differentiation to myofibroblasts, and less substrate contraction. In a full-thickness mouse wound model, treatment with films or meshes enables regeneration of pale thin tissues without scabs, dehydration, or tubercular scar formation. The epidermis of wounds treated with meshes develop small invaginations in the dermis within 2 weeks, indicating hair follicle and sweat gland regeneration. Consistent with the in vitro results, meshes reduce myofibroblast differentiation in vivo through downregulation of  $\alpha$ -SMA and TGF- $\beta$ 1, and upregulation of TGF- $\beta$ 3. The regenerated wounds treated with meshes are softer and more elastic than those treated with films. These results demonstrate that electrospun nanofibrous PHBV meshes mitigate excessive scar formation by regulating myofibroblast formation, showing their promise for use as wound dressings.

## Keywords

Elastomer, PHBV, electrospun nanofiber, scar formation, mechanical properties

Received: 21 June 2020; accepted: 23 July 2020

<sup>1</sup>Department of Biomedical Engineering, Columbia University, New York, NY, USA

<sup>2</sup>Institute of Tissue Regeneration Engineering, Dankook University, Cheonan, Republic of Korea

<sup>3</sup>State Key Laboratory of Microbial Resources, Institute of Microbiology, Chinese Academy of Sciences, Beijing, China

<sup>4</sup>College of Life Science, University of Chinese Academy of Sciences, Beijing, China

<sup>5</sup>Guangzhou Institute of Biomedicine and Health, Chinese Academy of Sciences, Guangzhou, China

<sup>6</sup>PLA Strategic Support Force Characteristic Medical Center, Beijing, China

\*Authors equally contributed to this work.

## Corresponding authors:

Hua Xiang, State Key Laboratory of Microbial Resources, Institute of Microbiology, Chinese Academy of Sciences, NO.1 Beichen West Road, Chaoyang District, Beijing 100101, China.  
Email: xiangh@im.ac.cn

Jing Han, State Key Laboratory of Microbial Resources, Institute of Microbiology, Chinese Academy of Sciences, NO.1 Beichen West Road, Chaoyang District, Beijing 100101, China.  
Email: hanjing@im.ac.cn



## Introduction

Following cutaneous injury, excessive scarring including formation of hypertrophic scars or keloids can cause pain and cosmetic disfigurement. An improved understanding of the role of mechanical tension in scar formation has led to treatments that target mechanical forces in wounds to minimize scarring.<sup>1</sup> Unlike adult wounds, fetal wounds heal without scars.<sup>2</sup> One reason for this phenomenon is that fetal wounds experience lower resting stress than adult wounds because fetal skin contains thinner collagen bundles. Increased mechanical stress in a wound induces scarring *via* mechanotransduction.<sup>3,4</sup> Dermal fibroblasts are critical in mechanosensing and mechanotransduction, converting mechanical cues to biochemical signals that promote scarring.<sup>5,6</sup> Clinical treatments that modulate the mechanical force in wounds can reduce scarring. For example, silicone gel sheets, silicone gel sheet-based polymer dressings, and paper tapes use mechanomodulation to improve wound healing outcomes. Silicone gel-based dressings reduce tensile stress in the wound and also minimize contraction by hydrating the stratum corneum.<sup>7,8</sup> Paper tape reduces tension when applied to the wound edge,<sup>9,10</sup> and paper tape containing micropores has been shown to reduce hypertrophic scarring in a rabbit ear model.<sup>10</sup>

Electrospun nanofibrous meshes are promising wound dressing materials because their elastic fibrous networks and high porosity resemble the extracellular matrix of skin.<sup>11,12</sup> Nanofibrous meshes provide greater mechanical support for cell attachment and migration than hydrogels, and are sufficiently porous to allow cell infiltration and cell-cell interactions.<sup>13,14</sup> In addition, nanofibrous meshes maintain wound hydration by absorbing wound exudates, further reducing contraction.<sup>15</sup> The mechanical features of nanofibrous meshes—including their stiffness, elasticity, and stress-relaxation rate—contribute to their therapeutic efficacy and can be tailored to balance the acceleration of wound closure and the functionality of the regenerated skin. Randomly-oriented electrospun microfibrillar scaffolds composed of elastomers such as poly(L-lactide-*co*-ε-caprolactone) and polyurethane have been engineered to reduce scarring by preventing stiffening of the regenerated skin tissue.<sup>16,17</sup>

Polyhydroxyalkanoates (PHAs) are an emerging class of natural polymers generated from bacteria or haloarchaea through unbalanced growth conditions.<sup>18</sup> The two types of PHAs, poly-3-hydroxybutyrate (PHB) and poly(3-hydroxybutyrate-*co*-3-hydroxyvalerate) (PHBV), have shown their potentials in a wide spectrum of biomedical applications, from drug delivery to tissue engineering.<sup>19–21</sup> Especially because of the incorporation of 3-hydroxyvalerate (3HV), PHBV holds many advantages over PHB in use particular for wound dressings, such as its lower crystallinity, greater elasticity and improved processability.<sup>22</sup> Despite many studies showing the possibility of

using either solution-cast PHBV films or electrospun PHBV fibers to promote wound healing, the 3HV content of these reported PHBV polymers was only ~10 mol% or less.<sup>12,23–29</sup> Low amount of 3HV content would lead to high crystallinity, which made PHBV polymer stiff and hydrophobic.<sup>30,31</sup> Consequently, additional coating or surface modification were needed in those studies. Moreover, the reported dressings were all made by bacterial PHBVs, known to have high level endotoxins. This would hinder their clinical translation as the endotoxins may induced undesired inflammation at the wound site.<sup>32</sup>

Our group was the first one, which developed methods to synthesize PHBV polymers with a wide range of 3HV content (10–60 mol%) using haloarchaea as a cell factory.<sup>33</sup> We previously showed that, with 30–60 mol% 3HV, the elongation at break of PHBV increased by over 400%, while it was only 5% for PHBV with 10 mol% 3HV.<sup>33</sup> We recently reported that haloarchaea-produced PHBV scaffolds demonstrated favorable mechanical strength, elasticity, biodegradability and biocompatibility compared with bacteria-produced PHAs published for biomedical applications.<sup>34,35</sup> These “tailored designs” of PHBV materials exhibited distinct thermal and mechanical properties with a range of biodegradation profiles and showed excellent *in vivo* biocompatibility.<sup>34–36</sup> Notably, the endotoxin concentration of our haloarchaea-produced PHBVs was 630-folds lower than that produced from bacteria.<sup>35</sup> Leveraging on these results, we hypothesized that haloarchaea-produced PHBV with higher 3HV content would be a better candidate as a wound dressing. In this study, we therefore used haloarchaea-produced PHBVs to fabricate both solution-cast films and electrospun nanofibrous meshes with different 3HV contents (10, 30 and 60 mol%; Figure 1). We first characterized their characteristics, and thermal and mechanical properties. We subsequently checked their inhibitory effects on preventing human dermal fibroblast (HDF) from its differentiation to myofibroblasts both *in vitro* and *in vivo*. Higher 3HV content in PHBV made the polymer more elastic and maintained minimal HDF/myofibroblast transition. As a result, the electrospun PHBV nanofibrous meshes mitigated excessive scar formation in the full-thickness wound mouse model.

## Materials and methods

### PHBV synthesis

*H. mediterranei* ES1 was used as a cell factory for production of three types PHBV with different 3HV content. The fermentation procedure and PHBV isolation from harvested cells were described in our previous study.<sup>33</sup> PHBV 10 was synthesized by using glucose (10 g/L) as the sole carbon source and PHBV 30 was synthesized by cofeeding glucose (10 g/L) with valerate (1.6 g/L) supplied at the beginning of culture. PHBV 60 polymer was synthesized by cofeeding glucose (10 g/L) with sequential

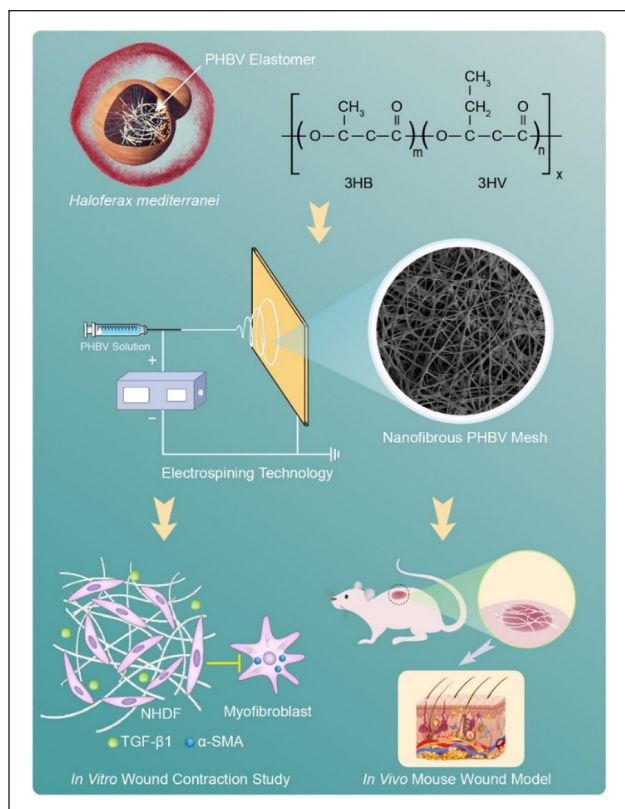


**Figure 1.** Schematic illustration of elastomeric nanofibrous PHBV meshes for preventing excessive scar formation. The biodegradable PHBV are produced by haloarchaeon *Haloferax mediterranei*. Electrospun nanofibrous meshes are fabricated using haloarchaea-produced PHBVs with distinct 3HV contents and mechanical properties. The effects of these scaffolds on reducing excessive scar formation are evaluated by culturing HDFs *in vitro* and by using a full-thickness wound mouse model *in vivo*, respectively.

valerate (0.8 g/L) supplying at 26 and 36 h of fermentation, respectively.

### Preparation of PHBV nanofibrous meshes and films

PHBVs were electrospun to create nanofibrous meshes. PHBVs were dissolved in chloroform at 1%, 2%, and 3% (w/v) PHBV 10, PHBV 30 and PHBV 60, respectively, according to their physical properties. The polymer solution was continuously injected using a 26G needle at a flow rate of 0.2 mL/h while electrospun by high voltage (15 kV). Electrospun PHBV nanofiber was collected on aluminum foil with a needle-to-collector distance of 10 cm. The nanofibrous meshes were dried for 1 week at room temperature to remove remaining solvents. To fabricate PHBV solution-cast films, PHBVs were dissolved in chloroform at 2% (w/v) and poured onto a glass dish as previously described. After complete evaporation of chloroform, the films were detached from the dish.

### Characterization of the PHBV scaffolds

The surface morphology and thickness of the PHBV scaffolds were determined by scanning electron microscopy (SEM; SU8010, Hitachi, Japan) and Image J (National Institute of Health). Each sample was mounted on an aluminum stump, coated with a layer of Pd/Pt alloy using an E-1045 ion sputter (Hitachi), and observed by SEM at an accelerating voltage of 5 kV. The fiber diameter was measured from different locations by ImageJ and its distribution was analyzed according to the histogram and the characteristic number of frequency distribution. The surface wettability of the scaffolds was evaluated by water contact angle measurement. The thermal properties of the scaffolds including glass transition temperature ( $T_g$ ), cool crystallization temperature ( $T_c$ ), melting temperature ( $T_m$ ), and melting enthalpy ( $\Delta H_m$ ), were measured by using differential scanning calorimetry (DSC; TA Instrument Q2000, USA) as described previously.<sup>1</sup> For mechanical property testing, scaffolds were cut into rectangles with 6 mm width and 10 cm length. Stress-strain measurements were conducted using an MTS Criterion™ Model 43 testing machine (MTS Systems Corporation, USA) at an extension rate of 5 mm/min at room temperature. The elongation at break, tensile strength, and Young's modulus were calculated using an MTS TestSuite TW software platform (MTS Systems Corporation).

### *In vitro* HDF culture

Human dermal fibroblasts (HDF) were cultured in DMEM supplemented with 10% FBS, Glutamax, non-essential amino acid, sodium pyruvate, and penicillin/streptomycin. HDFs were seeded on scaffolds at a density of  $10^5$  cells/cm<sup>2</sup>, and initial cell adhesion was evaluated by counting cells at 12 h after cell seeding. To observe cell morphology on scaffolds, cells were fixed with 2% (v/v) paraformaldehyde for 10 min, stained with Rhodamine-phalloidin and DAPI, and observed by fluorescence microscopy (Eclipse TE2000-U, Nikon, Japan). After 7 days of culture, the total DNA content of the cells was quantified by using a PicoGreen assay, and the fold cell expansion was calculated by comparing the DNA content at day 7 to that at day 1. HDF culture and analysis were conducted in three replicates.

### *In vitro* wound contraction study

HDFs were seeded at  $2 \times 10^5$  cells/cm<sup>2</sup> on PHBV scaffolds and on collagen gels as a control.<sup>37,38</sup> Collagen type I from rat tail (80 mL, 1.2 mg/mL in 0.6% (v/v) acetic acid) was mixed with  $10 \times$  DMEM (8.8 mL) and 5 M NaOH (1.2 mL) to adjust pH to neutral. Cell suspension ( $2 \times 10^5$  cells/10 mL) was mixed with pre-collagen gel and the mixture (100 mL) was added to a well of a 48-well plate. After solidifying for 1 h at 37°C, the gel was transferred to a 24-well plate and

medium was added. On the next day, the medium was changed to a contraction medium containing TGF- $\beta$ 1 (5 ng/mL) and the matrix contraction was monitored for 10 days. Changes in size of the scaffolds and collagen gels were analyzed by using Image J (National Institute of Health). On day 10 after contraction, cells seeded on scaffolds were fixed, permeabilized, and stained with mouse anti-human  $\alpha$ -SMA antibody (Abcam) for 12 h at 4°C, followed by incubation with Alexa Flour<sup>®</sup> 568 anti-mouse secondary antibody (Life Technologies) for 2 h at room temperature. Cell nuclei were stained with DAPI (Life Technologies). To assess  $\alpha$ -SMA expression in cells seeded on scaffolds, total RNA was extracted using Direct-zol RNA microprep kit (Zymo Research) and cDNA was synthesized using iScript cDNA synthesis kit (Bio-Rad). Real-time PCR analysis was performed using an ABI QuantStudio3 thermocycler and PowerUp SYBR Green Mater Mix (Thermo Fisher). The primers used for real-time PCR were the following:  $\alpha$ -SMA: 5'-CTG GGA CGA CAT GGA AAA-3' (forward) and 3'-ACA TGG CTG GGA CAT TGA-5' (reverse), GAPDH: 5'-GGA GCG AGA TCC CTC CAA AAT-3' (forward) and 5'-GGC TGT TGT CAT ACT TCT CAT GG-3' (reverse). Three replicates were performed for each sample.

### *In vivo wound healing study*

All mouse surgeries were approved by and performed in accordance with the guidelines from the ethics committee at the Chinese Academy of Sciences (APIMCAS2018056). Female C57BL/6 mice (10 weeks old) were first housed in groups of 6 for 2 weeks of adaptation. After this period, mice were anesthetized by 1% pentobarbital sodium and the back of mice were shaved. The back was then sterilized using alcohol (75% v/v). A 8-mm diameter skin wound of third-degree burn on the shaved back of mice was created using a metal brass rod and the burn was left for 2 days as described by Ibrahim et al.<sup>39</sup> Based on the in vitro performance, we tested the effects of PHBV 30 and 60 on scar formation in our in vivo study. The mice were then randomly assigned to the following groups ( $n=8$  per group): (1) untreated (negative control), (2) Tegaderm<sup>™</sup> (3M, USA, positive control), (3) PHBV 30 film, (4) PHBV 60 film, (5) PHBV 30 mesh, and (6) PHBV 60 mesh. The wounds were covered with sterile scaffolds (1 cm diameter circle) mentioned above and wrapped with elastic adhesive bandage (3M, USA) to fix the scaffolds. The wounds were imaged to calculate the percent open wound area by using Image J. The percentage of open wound area was calculated using equation 1.

$$\text{percentage open wound area (\%)} = 100 \times \frac{\text{wound area}_t}{\text{wound area}_0} \quad (1)$$

In equation 1, wound area<sub>t</sub> and wound area<sub>0</sub> represent the wound area at a specific time and the initial wound area,

respectively. On days 14 and 28 post-operation, the mice were euthanized by cervical dislocation and the regenerated tissues were collected for the analyses described below.

### *Mechanical tests of the regenerated wound*

On day 28 post-treatment, the regenerated tissues collected from mice were cut into 0.5×1 cm rectangles for mechanical analysis. For each group, four samples were prepared for the stress-strain measurements which were performed at room temperature at an extension rate of 2 mm/min using a dynamic mechanical analyzer (Discovery DMA 850, TA Instruments, USA). Strain and elongation modulus were obtained by stress-strain analysis.

### *Histological analysis*

The regenerated tissues were fixed in 10% neutral formalin for at least 48 h. A graded series of ethanol solutions were used for sample dehydration. Afterwards, wound tissues were embedded in paraffin followed by microtome sectioning into 4  $\mu$ m sections. Sections were stained for hematoxylin & eosin or Masson's trichrome (Masson Stain Kit, Yeasen, China). Sections for immunohistochemical analysis were treated using the EnVision two-step method (DS-0001 Polymer, CSGB-BIO, China). After dewaxing and dehydration, sections were incubated with anti-cytokeratin antibody (AE1/AE3) for 1 h at 37°C. After washing with PBS, sections were incubated with biotinylated goat anti-rabbit (CSGB-BIO) for 20 min at room temperature. Then sections were incubated with DAB (CSGB-BIO) for 5 min and quickly dipped into hematoxylin solutions for 20 s. After counterstaining, sections were rinsed in running tap water and dehydrated adequately. Images were acquired using an optical microscope (Olympus BX50, Olympus, Japan).

### *Real-time PCR*

The total RNA of regenerated tissues was extracted using an RNA Purification Kit (GMbiolab Co., Ltd, China), and cDNA was synthesized using random hexamers and MLV Reverse Transcriptase (Promega, USA). Primers used for real-time PCR were the following:  $\alpha$ -SMA: 5'-GAG CTA CGA ACT GCC TGA CG-3' (forward) and 5'-TAC CCC CTG ACA GGA CGT TG-3' (reverse), TGF- $\beta$ 1: 5'-TAC CAT GCC AAC TTC TGT CTG GGA-3' (forward) and 5'-ATG TTG GAC AAC TGC TCC ACC TTG-3' (reverse),  $\beta$ -actin: 5'-TGG ATC GGT TCC ATC CTG G-3' (forward) and 5'-GCA GCT CAG TAA CAG TCC GCC TAG-3' (reverse). Fluorogenic quantitative PCR was performed using a KAPA SYBR<sup>®</sup> FAST kit and was analyzed using a ViiATM 7 Real-Time PCR System (Applied Biosystems, Inc., USA). Fold changes in gene expression were calculated using the  $2^{-\Delta\Delta Ct}$  method, using  $\beta$ -actin as an endogenous control.

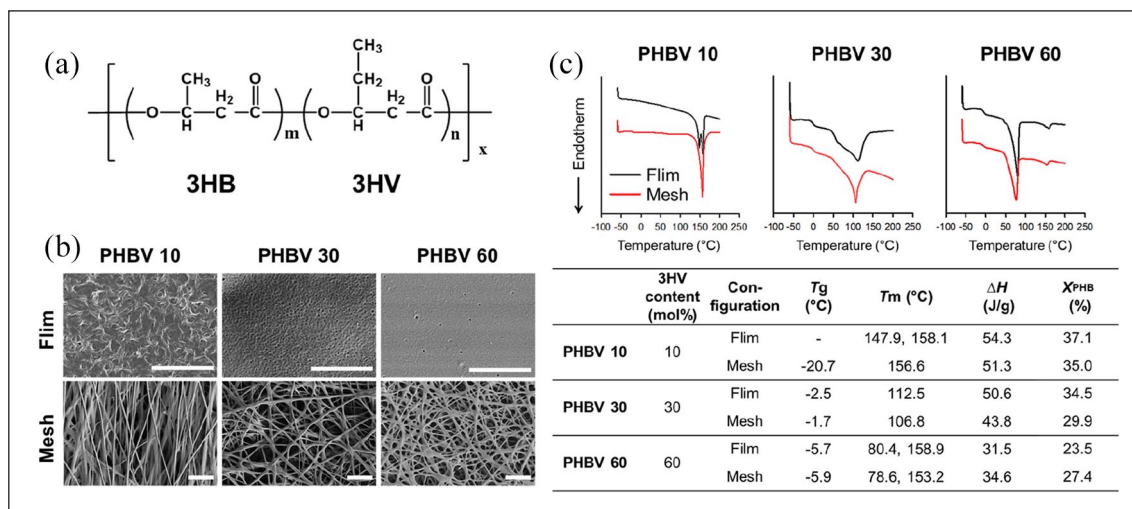


**Figure 2.** Morphological and thermal properties of PHBV solution-cast films and electrospun nanofibrous meshes. (a) Chemical structure of the random polymer PHBV. Three PHBV polymers with 10, 30, and 60 mol% 3HV were used. (b) SEM images (scale bar, 10  $\mu$ m). (c) DSC curves and thermal properties.

### Statistical analysis

Data was analyzed with GraphPad Prism™ software and shown as means  $\pm$  standard deviation (SD). One-way ANOVA was used to analyze the statistical significance at three significance level ( $*p < 0.05$ ).

## Results

### Characteristics of PHBV solution-cast films and electrospun nanofibrous meshes

Three halophilic archaea-produced PHBV polymers, with different 3HV contents of 10, 30, and 60 mol%, were used in this study (termed PHBV 10, PHBV 30, and PHBV 60, respectively, Figure 2(a)). The monomers 3HB (3-hydroxybutyrate) and 3HV are arranged randomly in the PHBV polymer chain. Since the PHBV polymers have different crystallinity, viscosity and molecular weight (PHBV 10: 1560 kDa, PHBV 30: 1730 kDa, and PHBV 60: 980 kDa), the concentration of polymer solution was adjusted accordingly for electrospinning. PHBV 10 is a rigid polymer due to its high crystallinity, and resulted in poor electrospinning when ejected as fibers and deposited onto the collector (Supplemental Figure 1). The morphologies of PHBV solution-cast films and electrospun nanofibrous meshes were observed under scanning electron microscopy (SEM) (Figure 2(b)). The average thickness of PHBV films was uniform ( $\sim 30 \mu$ m) across different 3HV conditions. For nanofibrous meshes, it was  $\sim 25 \mu$ m for PHBV 10 and  $10 \mu$ m for both PHBV 30 and 60 meshes (Supplemental Figure 2). The PHBV films showed a typical two-dimensional structure; nanofibrous meshes exhibited a more complex three-dimensional structure. As 3HV content increased, the PHBV film surface became smoother

because of decreasing polymer crystallinity. In contrast, electrospun PHBV meshes possessed highly uniform and smooth fibers. Fibers fabricated using PHBV 30 and 60 were more randomly-oriented than those formed using PHBV 10. The average fiber diameters in our meshes were  $567.3 \pm 196.7$  nm,  $780.0 \pm 255.0$  nm, and  $706.7 \pm 199.2$  nm for PHBV 10, 30, and 60, respectively (Supplemental Figure 3). These results showed that the PHBV nanofiber mesh formed by electrospinning PHBV 30 or 60 possessed a randomly-oriented, fibrillar matrix resembling the extracellular matrix (ECM) in the skin.

Water contact angle analysis was performed to measure the surface hydrophilicity of the fabricated films and fibrous meshes (Figure 3(a) and Supplemental Figure 4). PHBV 10 films and meshes showed similar water contact angles ( $91.6 \pm 2.6^\circ$  and  $93.8 \pm 1.1^\circ$ , respectively). In contrast, PHBV 30 and 60 meshes exhibited significantly lower water contact angles than their film counterparts ( $66.3 \pm 5.1^\circ$  vs  $85.5 \pm 3.1^\circ$  and  $51.5 \pm 4.2^\circ$  vs  $79.5 \pm 4.6^\circ$ ), indicating that different configurations (films or electrospun meshes) of the same PHBV 30 and 60 polymer resulted in distinct surface characteristics.

### Thermal properties of PHBV solution-cast films and electrospun nanofibrous meshes

We next characterized the thermal properties of the PHBV films and nanofibrous meshes by using differential scanning calorimetry (DSC) (Figure 2(c)). All DSC heating curves exhibited no crystallization temperature ( $T_c$ ) peak, indicating that equilibrium crystallinity had been reached. The electrospinning and film cast methods differed in their effects on polymer crystal formation: the PHBV 10 film showed one melting domain with a doublet at  $147.92^\circ\text{C}$

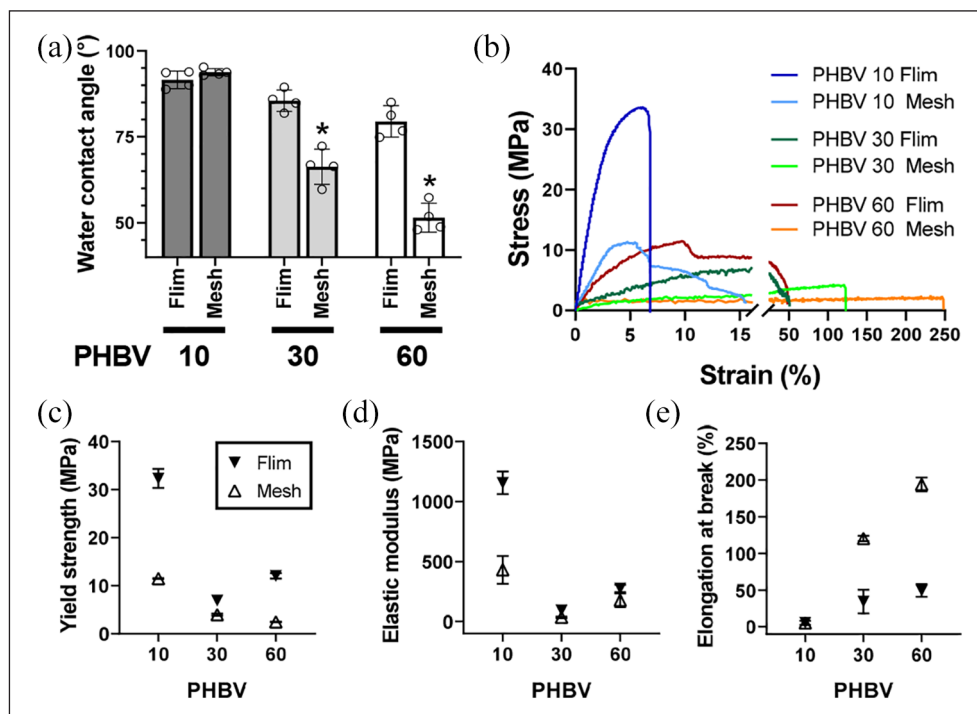


**Figure 3.** Surface and mechanical properties of PHBV solution-cast films and electrospun nanofibrous meshes. (a) Water contact angles. \* $p < 0.05$  by one-way ANOVA. (b–e) Mechanical analysis of scaffolds: stress-strain curves (b), yield strength (c), elastic modulus (d), and elongation at break (e).

and 158.05°C, suggesting that it formed two distinct crystalline states; in contrast, the PHBV 10 mesh showed a single melting peak at 156.55°C, indicating a single crystalline state. When 3HV content was increased to 30 mol% (PHBV 30), both films and meshes showed a broad melting endotherm from 50–150°C, indicating that the 3HV and 3HB segments had excellent blend compatibility. However, at 60 mol% 3HV (PHBV 60), two melting domains were observed, with peaks at 80°C and 159°C, indicating separate 3HV and 3HB crystallization phases. The higher temperature melting domain represented the 3HB crystallization lattice; the lower temperature melting domain represented the 3HV crystallization lattice. Thus, different configurations (film or electrospun mesh) of the same PHBV polymer possessed different wettability and crystallinity. The crystallinity of PHBV 10 and 30 films was 37.1% and 34.5%, respectively—higher than that of the corresponding fibrous meshes (35.0% and 29.9%, respectively). PHBV 60 showed the opposite trend, with greater crystallinity in the film (23.5%) than in the mesh (27.4%). Taken together, these results showed that electrospun PHBV fibrous meshes had different thermal properties compared with the solution-cast film counterparts.

### Mechanical properties of PHBV solution-cast films and electrospun nanofibrous meshes

The mechanical properties of our PHBV films and meshes were analyzed using MTS Criterion Model 43. As shown

in Figure 3(b), the films showed higher yield strength and elastic modulus than the nanofiber meshes (Figure 3(c) and (d)). In contrast, the elongation at break of PHBV 30 and 60 meshes were 117.8% and 194%, respectively—3.4- and 3.9-times higher when compared with the corresponding films (34.2% and 49.4%) (Figure 3(e)). The yield strength of PHBV meshes decreased with increasing 3HV from 10 to 60 mol%, whereas the elongation at break increased; PHBV 60 meshes had higher elongation at break than PHBV 10 or 30, indicating that the polymer became more elastic with increasing 3HV content. Thus, electrospinning the polymer into nanofibrous meshes improved its mechanical stability, an important characteristic for withstanding physiological strains during wound recovery.

### HDF culture on PHBV substrates in vitro

To test the effect of PHBV substrate architecture on cell adhesion and proliferation, HDFs were seeded on either PHBV films or meshes (Figure 4). At 12 h post-seeding, cell attachment on the electrospun mesh was better than that on the solution-cast film counterpart, and increasing 3HV content gave a positive effect on cell attachment (Figure 4(a)). When cells were seeded on the relatively hydrophobic PHBV 10 film, HDF cells tended to aggregate; as 3HV content in the films increased (and thus hydrophilicity, Figure 3(a)), they spread out rather than aggregated (Figure 4(c)). In contrast, a well-spread cell

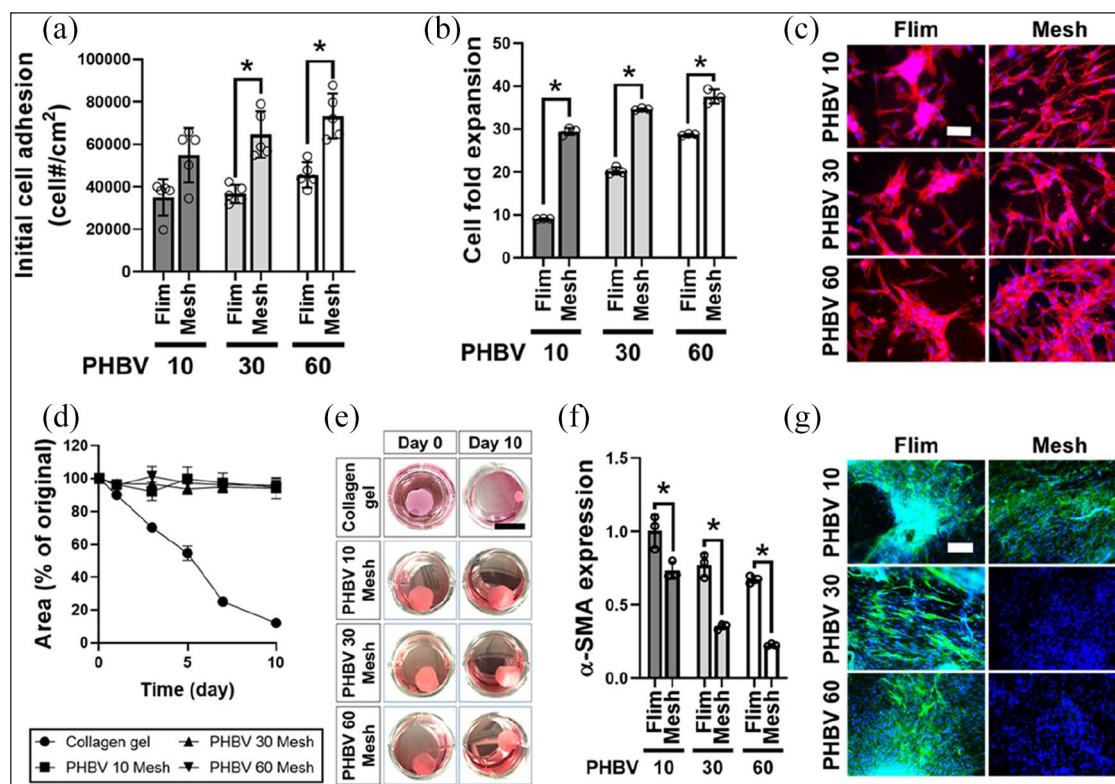


**Figure 4.** In vitro HDF culture on PHBV films or nanofibrous meshes (NF). (a) Cell adhesion on PHBV scaffolds after 12h. (b) Cell fold-expansion after 7 days of culture. (c) Cell morphology on PHBV scaffolds 12h after seeding. Overlay of DAPI (blue) and F-actin (green) images (scale bar, 100  $\mu$ m). (d-e) Analysis of contraction of collagen gels and PHBV meshes. Surface area changes (d) were evaluated by comparing sizes at days 0 and 10 in images (e) (scale bar, 1 cm). (f)  $\alpha$ -SMA expression in cells cultured on PHBV scaffolds for 7 days. (g) Fluorescence images of cells on scaffolds stained with anti- $\alpha$ -SMA antibody (green) and DAPI (blue) (scale bar, 200  $\mu$ m). \* $p < 0.05$  by one-way ANOVA.

morphology was observed on all three nanofibrous meshes regardless of 3HV content. In this 1-week-long in vitro culture, HDF cells proliferated faster on the PHBV 60 film compared with other groups. For electrospun meshes, all three PHBVs supported greater cell proliferation than their film counterparts (Figure 4(b)).

In vitro scar-related outcomes were evaluated by comparing PHBV films and meshes to collagen gels. The collagen-based cell contraction assay is the gold-standard for in vitro wound contraction studies because fibroblasts and myofibroblasts in collagen gels closely mimic in vivo cell behavior in healing scars.<sup>40-42</sup> Thus, we used HDF-seeded collagen gel as a model of fibroblast-driven matrix contraction and myofibroblast formation in untreated wounds. HDFs were seeded in collagen gel or PHBV nanofibrous meshes or on PHBV films. The contraction of the cell/substrate composites was monitored for 10 days. Since wound contraction force is from myofibroblasts, HDFs-seeded substrates were treated with transforming growth factor-beta 1 (TGF- $\beta$ 1) to induce the fibroblast transition to myofibroblasts. The area of the PHBV meshes and films was reduced due to contraction by  $\sim$ 6% over 10 days; in contrast, the area of collagen gels was reduced by  $\sim$ 88%

(Figure 4(d) and (e) and Supplemental Figure 5). The mitigated contraction implied that there was less HDF/myofibroblast transition in the PHBV mesh and film groups. Lower expression of alpha-smooth muscle actin ( $\alpha$ -SMA) in the cells of the PHBV mesh groups gave an evidence of less HDF/myofibroblast transition compared to the film counterparts (Figure 4(f)). Immunohistochemical staining supported the real-time PCR result, showing that significantly less  $\alpha$ -SMA was present in the cells seeded on PHBV 30 and 60 meshes than in the cells on the corresponding films (Figure 4(g)). These results showed that electrospun PHBV 30 and 60 nanofibrous meshes reduced myofibroblast conversion in vitro.

### Effects of PHBV scaffolds on wound healing in vivo

To validate the wound healing capability of the proposed PHBV dressings, we established a full-thickness wound mouse model by creating a third-degree burn on the shaved back of mice. The wounds were covered with either PHBV films, nanofibrous PHBV meshes, or 3M Tegaderm<sup>TM</sup>, followed by a sterile bandage; an untreated group was covered

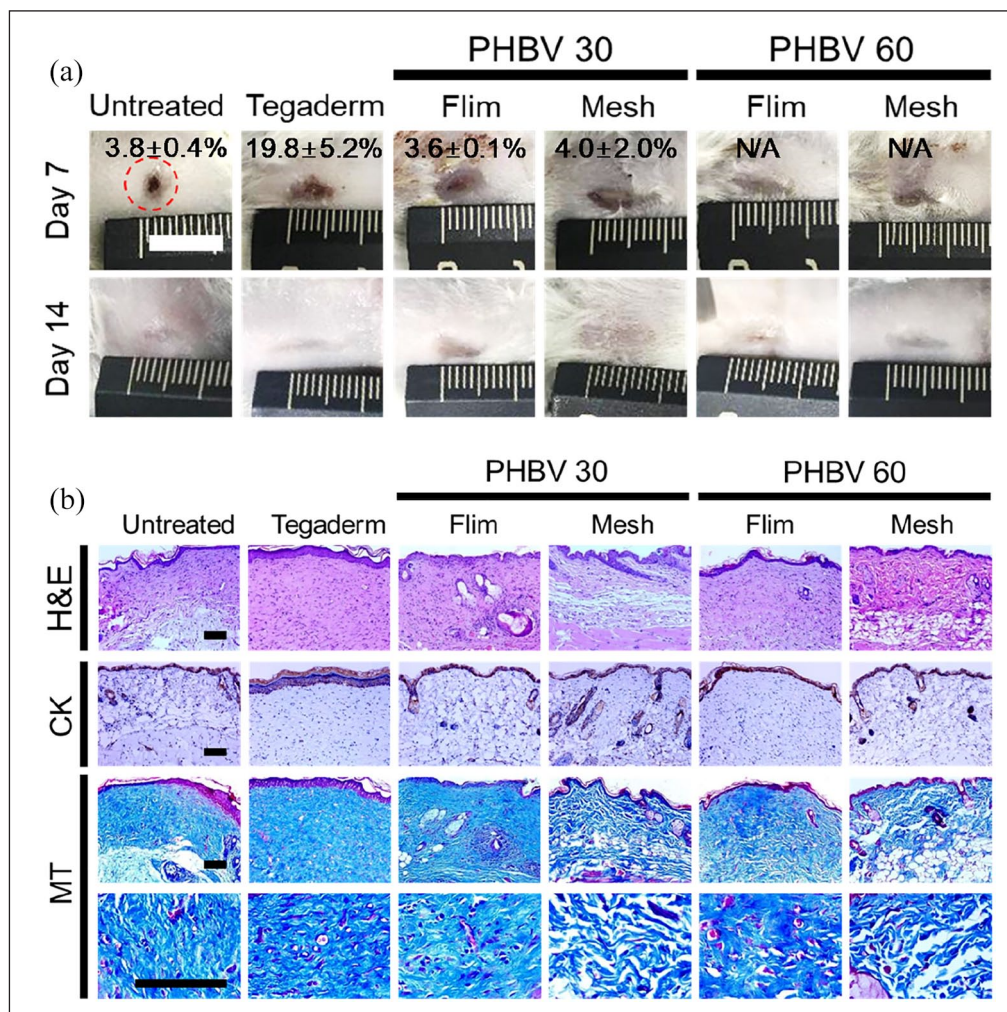


**Figure 5.** Wound regeneration in a full-thickness in vivo mouse wound model. Wounds were treated with PHBV 30 and PHBV 60 scaffolds (film or mesh), or with Tegaderm™ (positive control). (a) Gross appearance of wounds, indicating open wound areas (%) at days 7 and 14 after wound dressing (scale bar, 1 cm). (b) Histological analysis of regenerated wounds at day 28, staining with H&E, anti-cytokeratin antibody (CK), and Masson's trichrome (MT) (scale bar, 100  $\mu$ m).

\* $p < 0.05$  by one-way ANOVA.

with only a sterile bandage. Tegaderm™, a commercial medical dressing, is a polyurethane membrane coated with a layer of an acrylic adhesive, which does not contain any bioactive molecules. It mechanically supports wounds during the regeneration just like the PHBV scaffolds. To focus on how the topographical and mechanical properties of PHBV scaffolds affect the wound healing and reduction of scar formation, Tegaderm™ was used as a positive control. Since PHBV 10 did not significantly affect myofibroblast conversion and activity in vitro (Figure 4(f) and (g)), only the films and meshes generated from PHBV 30 and 60 were used in the in vivo validation. Wound healing was monitored and evaluated by gross observation, histological examination, mechanical testing, and by analyzing the expression of scarring-associated molecular markers (Figures 5 and 6).

At Day 7, the untreated wounds were almost closed due to severe contraction caused by dehydration, and were

covered with stiff scabs (Figure 5(a)). Tegaderm treatment reduced wound contraction, but the open wound area was larger than the PHBV-treated groups. Wounds treated with PHBV films and meshes showed regeneration of pale and thin tissues, and did not exhibit scabs, contraction, or tubercular scar formation. At Day 14, overall wound closure was complete in all the groups, and there was no significant difference in the appearance between groups. Histological staining showed that at Day 28, the epidermal-dermal interface of the untreated, Tegaderm, and PHBV film groups was relatively flat; in contrast, the epidermis of the PHBV nanofibrous mesh groups developed small invaginations into the dermis, indicating the beginning of hair follicle or sweat gland regeneration (Figure 5(b)). Wounds treated with PHBV meshes also exhibited an ordered arrangement of collagen fibers, whereas the untreated, Tegaderm, and PHBV film wounds showed

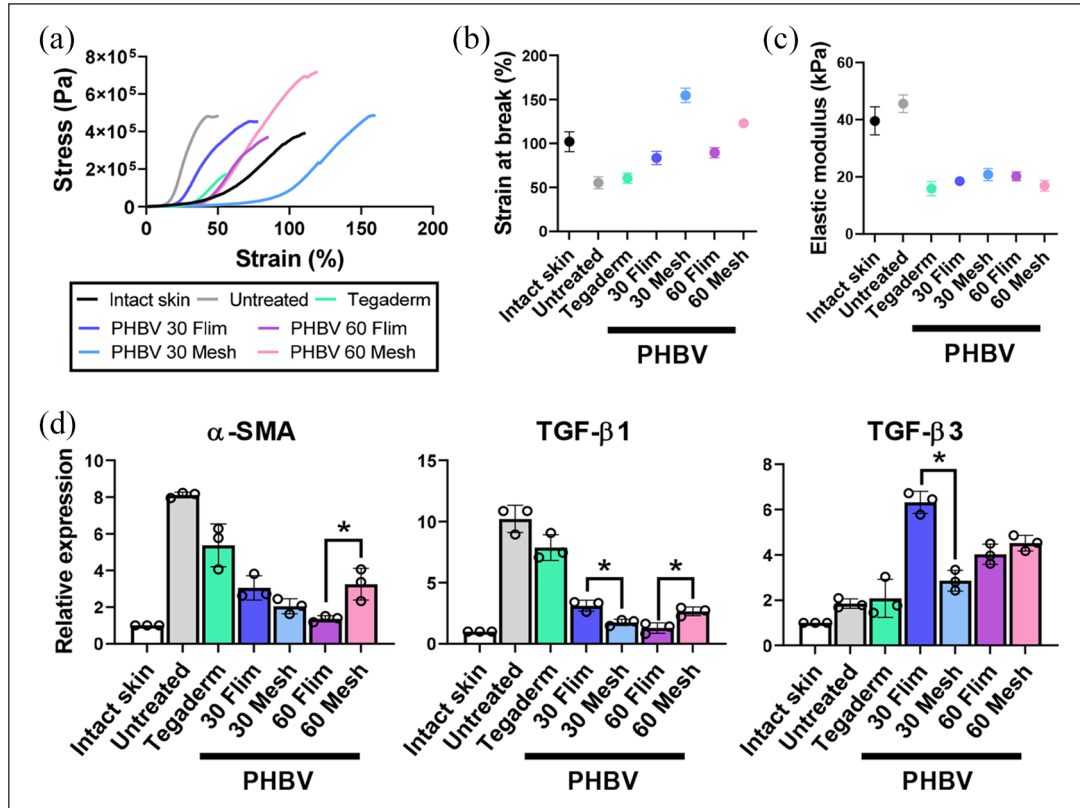


**Figure 6.** Effect of PHBV scaffolds on wound healing and scarring at 28 days after treatment: (a–c) Mechanical properties of regenerated wounds: stress-strain curves (a), strain at break (b), and elastic modulus (c). For each group, three independent samples were used for the stress-strain measurements and one representative result was presented. (d) Expression of scarring-associated markers ( $\alpha$ -SMA, TGF- $\beta$ 1, and TGF- $\beta$ 3) in regenerated wounds. \* $p < 0.05$  by one-way ANOVA.

disordered collagen fibers. These suggested that our PHBV nanofibrous meshes caused better re-epithelialization of the skin than the PHBV films.

To further evaluate wound regeneration and scar formation, the re-epithelialized tissues were harvested at Day 28 and subjected to static tensile testing until failure (Figure 6(a–c)). Intact mouse skin withstood strains up to around 100%, whereas untreated wounds withstood strains up to only 50%. The elastic modulus of re-epithelialized untreated wounds (45.6 kPa) was greater than that of intact skin (39.6 kPa); all other groups exhibited much lower elastic modulus (10–20 kPa). The PHBV film and mesh groups exhibited higher strain levels at breakage (80–150%) than the untreated and Tegaderm-treated groups. The maximum strains for PHBV 30 and 60 film groups were 80% and 90%, respectively; those of PHBV 30 and 60 mesh groups were 150% and 130%—1.9- and 1.4-fold greater than their film counterparts, respectively. These results indicated that the regenerated wounds treated with PHBV nanofibrous meshes were more elastic and softer than those treated with PHBV films. We then checked the myofibroblast differentiation markers ( $\alpha$ -SMA and TGF- $\beta$ 1); expression levels of  $\alpha$ -SMA and TGF- $\beta$ 1 (indicators

of myofibroblast differentiation) in wounds treated with PHBV films and meshes were significantly lower than in untreated and Tegaderm-treated wounds (Figure 6(d)). The PHBV films and meshes also caused an increase in expression of TGF- $\beta$ 3, a cytokine involved in inhibiting scar formation. Similar to what we observed in vitro, the PHBV scaffolds reduced myofibroblast differentiation in vivo by modulating scarring-associated cytokine expression.

## Discussion

There are multiple factors that influence the outcome of wound healing. Scar contraction is one of the major factors, and it can occur for as long as 18 months during wound healing.<sup>1</sup> Biomaterial longevity is thus an important factor for mitigating wound scar formation.<sup>16,17</sup> A slow degradation rate is vital for biomaterial scaffolds that prevent scar contraction.<sup>43</sup> In a previous study, we evaluated the degradation behavior of haloarchaea-producing PHBV polymers following implantation in the rabbit dorsal subcutis.<sup>34</sup> PHBV films with 30 and 60 mol% 3HV showed a slow degradation rate of roughly 6 months, allowing these films to maintain intact throughout wound healing in this

model. In the current study, the electrospun PHBV 30 and 60 nanofibrous meshes are more elastic than PHBV 30 and 60 films due to their fibrous network architecture and possess sufficient mechanical stability to withstand wound contraction.

Surface wettability is important for material design for wound healing as it plays a role in cell-material interactions. Wettability contributes to serum protein adsorption and induces cell adhesion.<sup>44</sup> Moderate hydrophilicity is preferable for cell adhesion and growth; surfaces that are super-hydrophilic (contact angle  $<5^\circ$ ) or super-hydrophobic (contact angle  $>150^\circ$ ) are unsuitable for cell attachment and growth.<sup>45</sup> The contact angles of all PHBV films and nanofibers meshes are between  $5^\circ$  and  $150^\circ$ . Compared with the film counterparts, PHBV 30 and 60 nanofibrous meshes exhibit lower contact angles, which enables greater cell attachment and proliferation. Various factors affect the surface wettability of polymeric scaffolds, including porosity, roughness, and the hydrophobicity of the polymer used to create the scaffold.<sup>45,46</sup> Electrospinning polymers creates a porous scaffold with fibers stacked on a collector, resulting in an interconnected fibrous network.<sup>47</sup> For PHBV polymers, higher 3HV contents results in greater hydrophilicity, lower crystallinity, and smoother surfaces. The electrospun PHBV 60 fibrous meshes exhibit the greatest wettability and cell adhesion and proliferation among all groups, suggesting that this polymer architecture enhances biocompatibility. These results are consistent with the results reported by Suwantong et al. that fibrous PHBV (with 5 mol% 3HV) mats better support mouse fibroblast L929 proliferation than the PHBV film counterparts.<sup>30</sup> Kuppen et al. showed that PHBV (with 8% 3HV) fibers possess higher porosity and ductility than films. Human skin fibroblasts seeded on the PHBV (with 8% 3HV) fibers also grow with faster proliferation rate than those seeded on the film counterpart.<sup>29</sup>

Wound contraction can cause scar formation, poor tissue mobility, and functional impairment,<sup>48</sup> and it is mainly driven by myofibroblast, which produces excessive matrix and generate internal contraction forces that lead to scar contracture. TGF- $\beta$ 1 plays an important role in myofibroblast formation and subsequent over-accumulation of ECM and scar formation.<sup>49–51</sup> After fibroblast is converted to myofibroblast, it expresses  $\alpha$ -SMA and acquires a contractile phenotype.<sup>52</sup> In our *in vivo* experiments, treatment with electrospun PHBV meshes reduce the expression of  $\alpha$ -SMA and TGF- $\beta$ 1 and increase TGF- $\beta$ 3 expression in the wound. These results indicate that PHBV meshes reduce myofibroblast differentiation and excessive scarring by reducing the mechanical stress in the wound. Conversion of fibroblasts into myofibroblasts is highly dependent on the stiffness of adjacent tissue *in vivo* and on the stiffness of scaffolds *in vitro*.<sup>7,53</sup> Increased mechanical stress in the wound environment induces scarring *via* mechanotransduction.<sup>54</sup> It is important to reduce mechanical force in the wound to prevent excessive scarring. Electrospun PHBV

meshes have greater ductility than solution-cast films and are thus able to distribute contraction forces better than films. The fibrous network structure of the mesh results in elasticity and tenacity (resistance to deformation), which help the injured tissue withstand stretching or compression. PHBV 60 is more elastic when fabricated as a nanofibrous mesh than as a film, and it prevents wound contraction caused by myofibroblast formation. Only wounds treated with PHBV 30 and 60 meshes exhibit invagination of the epidermis into the dermis, indicating accelerated development of hair follicles and sweat glands. In addition, more ordered collagen fibers are observed in the wounds treated with PHBV meshes than in the wounds treated with PHBV films or Tegaderm. The interlaced network of the mesh is highly porous, allowing cell infiltration and migration into the wound. The fibrous structure not only supports cell attachment and migration, but also induces orderly ECM deposition. Although PHBV-based scaffolds cannot completely reconstruct the skin tissues and prevent scar formation due to a lack of biochemical cues,<sup>55</sup> we believe PHBV nanofibrous meshes with a 3HV content of 30–60 mol% are promising materials for wound healing applications due to their superior mechanical offloading, mechanomodulation, biocompatibility, and slow degradation.

## Conclusion

In summary, this study is the first effort in the field on evaluating the effects of PHBV nanofibrous meshes containing a high 3HV content (30 and 60 mol%) for wound dressing. Our elastomeric nanofibrous PHBV meshes exhibit intermingled fibrous structures with high porosity and great elasticity. HDF cell attachment and proliferation are significantly improved on the nanofibrous PHBV meshes in comparison with that on the solution-cast films. Furthermore, on nanofibrous PHBV meshes, we observe less myofibroblast differentiation and substrate contraction. In an *in vivo* full-thickness mouse wound model, PHBV nanofibrous meshes not only improve re-epithelization of the wounds, but also mitigate severe wound contraction. Thus, the subsequent excessive scar formation is expected to be reduced due to regulation of myofibroblast formation. Taken together, the electrospun nanofibrous PHBV meshes show a great promise for the use as wound dressings.

## Acknowledgements

The authors thank the assistance from Chunli Li (Public Technology Service Center of Institute of Microbiology, CAS) in SEM observation, Yeh-Hsing Lao (Columbia University) in manuscript preparation, and Yuanyuan Bei and Sitong Liu in scheme design.

## Declaration of conflicting interests

The author(s) declared no potential conflicts of interest with respect to the research, authorship, and/or publication of this article.

## Funding

The author(s) disclosed receipt of the following financial support for the research, authorship, and/or publication of this article: Funding from the National Key R&D Program of China (No. 2018YFA0900200), the National Natural Science Foundation of China (No. 31970031 and No. 91751201), National Key R&D Program of China (No. 2019YFA0110500), and Basic Science Research Program (Korean NRF: 2016R1A6A3A03012178).

## ORCID iD

Jing Han  <https://orcid.org/0000-0002-9207-0238>

## Supplemental material

Supplemental material for this article is available online.

## References

- Aarabi S, Bhatt KA, Shi Y, et al. Mechanical load initiates hypertrophic scar formation through decreased cellular apoptosis. *FASEB J* 2007; 21: 3250–3261.
- Lo DD, Zimmermann AS, Nauta A, et al. Scarless fetal skin wound healing update. *Birth Defects Res C* 2012; 96: 237–247.
- Gurtner GC, Dauskardt RH, Wong VW, et al. Improving cutaneous scar formation by controlling the mechanical environment large animal and phase I studies. *Ann Surg* 2011; 254: 217–225.
- Wang N, Tytell JD and Ingber DE. Mechanotransduction at a distance: mechanically coupling the extracellular matrix with the nucleus. *Nat Rev Mol Cell Bio* 2009; 10: 75–82.
- Kadi A, Fawzi-Grancher S, Lakisic G, et al. Effect of cyclic stretching and TGF-beta on the SMAD pathway in fibroblasts. *Bio-Med Mater Eng* 2008; 18: S77–S86.
- Chiquet M, Tunc-Civelek V and Sarasa-Renedo A. Gene regulation by mechanotransduction in fibroblasts. *Appl Physiol Nutr Me* 2007; 32: 967–973.
- Khan U and Bayat A. Microarchitectural analysis of decellularised unscarred and scarred dermis provides insight into the organisation and ultrastructure of the human skin with implications for future dermal substitute scaffold design. *J Tissue Eng* 2019; 10: 2041731419843710.
- Akaishi S, Akimoto M, Hyakusoku H, et al. The tensile reduction effects of silicone gel sheeting. *Plast Reconstr Surg* 2010; 126: 109e–111e.
- Atkinson JAM, McKenna KT, Barnett AG, et al. A randomized, controlled trial to determine the efficacy of paper tape in preventing hypertrophic scar formation in surgical incisions that traverse Langer's skin tension lines. *Plast Reconstr Surg* 2005; 116: 1648–1656.
- Rosengren H, Askew DA, Heal C, et al. Does taping torso scars following dermatologic surgery improve scar appearance? *Dermatol Pract Concept* 2013; 3: 75.
- Levin A, Sharma V, Hook L, et al. The importance of factorial design in tissue engineering and biomaterials science: optimisation of cell seeding efficiency on dermal scaffolds as a case study. *J Tissue Eng* 2018; 9: 2041731418781696.
- Pilehvar-Soltanahmadi Y, Akbarzadeh A, Moazzez-Lalaklo N, et al. An update on clinical applications of electrospun nanofibers for skin bioengineering. *Artif Cell Nanomed B* 2016; 44: 1350–1364.
- Wang X, Ding B and Li B. Biomimetic electrospun nanofibrous structures for tissue engineering. *Mater Today (Kidlington)* 2013; 16: 229–241.
- Kim HS, Sun X, Lee JH, et al. Advanced drug delivery systems and artificial skin grafts for skin wound healing. *Adv Drug Deliv Rev* 2019; 146: 209–239.
- Ousey K, Cutting KF, Rogers AA, et al. The importance of hydration in wound healing: reinvigorating the clinical perspective. *J Wound Care* 2016; 25: 122–130.
- Lorden ER, Miller KJ, Bashirov L, et al. Mitigation of hypertrophic scar contraction via an elastomeric biodegradable scaffold. *Biomaterials* 2015; 43: 61–70.
- Lorden ER, Miller KJ, Ibrahim MM, et al. Biostable electrospun microfibrillar scaffolds mitigate hypertrophic scar contraction in an immune-competent murine model. *Acta Biomater* 2016; 32: 100–109.
- Lee Y, Cho IJ, Choi SY, et al. Systems metabolic engineering strategies for non-natural microbial polyester production. *Biotechnol J* 2019; 14(9): 1800426.
- Wu Q, Wang Y and Chen GQ. Medical Application of microbial biopolyesters polyhydroxyalkanoates. *Artif Cell Blood Sub* 2009; 37: 1–12.
- Hokmabad VR, Davaran S, Ramazani A, et al. Design and fabrication of porous biodegradable scaffolds: a strategy for tissue engineering. *J Biomat Sci-Polym E* 2017; 28: 1797–1825.
- Rodriguez-Carmona E and Villaverde A. Nanostructured bacterial materials for innovative medicines. *Trends Microbiol* 2010; 18: 423–430.
- Gassner F and Owen AJ. Some properties of poly(3-hydroxybutyrate)-poly(3-hydroxyvalerate) blends. *Polym Int* 1996; 39: 215–219.
- Asencio IO, Mittar S, Sherborne C, et al. A methodology for the production of microfabricated electrospun membranes for the creation of new skin regeneration models. *J Tissue Eng* 2018; 9: 2041731418799851.
- Yuan J, Geng J, Xing ZC, et al. Novel wound dressing based on nanofibrous PHBV-keratin mats. *J Tissue Eng Regen M* 2015; 9: 1027–1035.
- Biazar E and Keshel SH. The healing effect of stem cells loaded in nanofibrous scaffolds on full thickness skin defects. *J Biomed Nanotechnol* 2013; 9: 1471–1482.
- Keshel SH, Biazar E, Tavirani MR, et al. The healing effect of unrestricted somatic stem cells loaded in collagen-modified nanofibrous PHBV scaffold on full-thickness skin defects. *Artif Cell Nanomed B* 2014; 42: 210–216.
- Zonari A, Cerqueira MT, Novikoff S, et al. Poly(hydroxybutyrate-co-hydroxyvalerate) bilayer skin tissue engineering constructs with improved epidermal rearrangement. *Macromol Biosci* 2014; 14: 977–990.
- Zeinali R, Biazar E, Keshel SH, et al. Regeneration of full-thickness skin defects using umbilical cord blood stem cells loaded into modified porous scaffolds. *Asaio J* 2014; 60: 106–114.
- Kuppan P, Vasanthan KS, Sundaramurthi D, et al. Development of poly(3-hydroxybutyrate-co-3-hydroxyvalerate) fibers for skin tissue engineering: effects of topography, mechanical, and chemical stimuli. *Biomacromolecules* 2011; 12: 3156–3165.

30. Suwantong O, Waleetorncheepsawat S, Sanchavanakit N, et al. *In vitro* biocompatibility of electrospun poly(3-hydroxybutyrate) and poly(3-hydroxybutyrate-co-3-hydroxyvalerate) fiber mats. *Int J Biol Macromol* 2007; 40: 217–223.
31. Lee IS, Kwon OH, Meng W, et al. Nanofabrication of microbial polyester by electrospinning promotes cell attachment. *Macromol Res* 2004; 12: 374–378.
32. Dinjaski N and Prieto MA. Smart polyhydroxyalkanoate nanobeads by protein based functionalization. *Nanomed Nanotechnol* 2015; 11: 885–899.
33. Han J, Wu LP, Hou J, et al. Biosynthesis, characterization, and hemostasis potential of tailor-made poly(3-hydroxybutyrate-co-3-hydroxyvalerate) produced by *Haloferax mediterranei*. *Biomacromolecules* 2015; 16: 578–588.
34. Han J, Wu L-P, Liu X-B, et al. Biodegradation and biocompatibility of haloarchaea-produced poly(3-hydroxybutyrate-co-3-hydroxyvalerate) copolymers. *Biomaterials* 2017; 139: 172–186.
35. Xue Q, Liu XB, Lao YH, et al. Anti-infective biomaterials with surface-decorated tachyplestin I. *Biomaterials* 2018; 178: 351–362.
36. Liu XB, Wu LP, Hou J, et al. Environmental biodegradation of haloarchaea-produced poly(3-hydroxybutyrate-co-3-hydroxyvalerate) in activated sludge. *Appl Microbiol Biot* 2016; 100: 6893–6902.
37. Hinz B, Celetta G, Tomasek JJ, et al. Alpha-smooth muscle actin expression upregulates fibroblast contractile activity. *Mol Biol Cell* 2001; 12: 2730–2741.
38. Levinson H, Hopper JE and Ehrlich HP. Overexpression of integrin  $\alpha v$  promotes human osteosarcoma cell populated collagen lattice contraction and cell migration. *J Cell Physiol* 2002; 193: 219–224.
39. Ibrahim MM, Bond J, Bergeron A, et al. A novel immune competent murine hypertrophic scar contracture model: a tool to elucidate disease mechanism and develop new therapies. *Wound Repair Regen* 2014; 22: 755–764.
40. Grinnell F and Lamke CR. Reorganization of hydrated collagen lattices by human-skin fibroblasts. *J Cell Sci* 1984; 66: 51–63.
41. Carlson MA and Longaker MT. The fibroblast-populated collagen matrix as a model of wound healing: a review of the evidence. *Wound Repair Regen* 2004; 12: 134–147.
42. Woeller CF, O'Loughlin CW, Roztocil E, et al. Salinomycin and other polyether ionophores are a new class of antiscarring agent. *J Biol Chem* 2015; 290: 3563–3575.
43. Yannas IV. Emerging rules for inducing organ regeneration. *Biomaterials* 2013; 34: 321–330.
44. Junkar I. Interaction of cells and platelets with biomaterial surfaces treated with gaseous plasma. *Adv Biomembr Lipid* 2016; 23: 25–59.
45. Chen LN, Yan C and Zheng ZJ. Functional polymer surfaces for controlling cell behaviors. *Mater Today* 2018; 21: 38–59.
46. Alves NM, Pashkuleva I, Reis RL, et al. Controlling cell behavior through the design of polymer surfaces. *Small* 2010; 6: 2208–2220.
47. Ng R, Zang R, Yang KK, et al. Three-dimensional fibrous scaffolds with microstructures and nanotextures for tissue engineering. *Rsc Adv* 2012; 2: 10110–10124.
48. van Zuijlen PPM, Ruurda JJB, van Veen HA, et al. Collagen morphology in human skin and scar tissue: no adaptations in response to mechanical loading at joints. *Burns* 2003; 29: 423–431.
49. Desmoulière A, Geinoz A, Gabbiani F, et al. Transforming growth factor-beta 1 induces alpha-smooth muscle actin expression in granulation tissue myofibroblasts and in quiescent and growing cultured fibroblasts. *J Cell Biol* 1993; 122: 103–111.
50. Chalmers RL. The evidence for the role of transforming growth factor-beta in the formation of abnormal scarring. *Int Wound J* 2011; 8: 218–223.
51. Bettinger DA, Yager DR, Diegelmann RF, et al. The effect of TGF-beta on keloid fibroblast proliferation and collagen synthesis. *Plast Reconstr Surg* 1996; 98: 827–833.
52. Peters T, Sindrilaru A, Hinz B, et al. Wound-healing defect of CD18(-/-) mice due to a decrease in TGF-beta(1) and myofibroblast differentiation. *Embo J* 2005; 24: 3400–3410.
53. da Cunha CB, Klumpers DD, Li WA, et al. Influence of the stiffness of three-dimensional alginate/collagen-I interpenetrating networks on fibroblast biology. *Biomaterials* 2014; 35: 8927–8936.
54. Barnes LA, Marshall CD, Leavitt T, et al. Mechanical forces in cutaneous wound healing: emerging therapies to minimize scar formation. *Adv Wound Care* 2018; 7: 47–56.
55. Robert AW, Azevedo Gomes F, Rode MP, et al. The skin regeneration potential of a pro-angiogenic secretome from human skin-derived multipotent stromal cells. *J Tissue Eng* 2019; 10: 2041731419833391.